FGC 1287 and its enigmatic 250 kpc long HI tail in the outskirts of Abell 1367

T. C. Scott[1][*], L. Cortese[2,3], P. Lagos[1], E. Brinks[4], A. Finoguenov[5] and L. Coccato [6]

[1] *Institute of Astrophysics and Space Sciences (IA), Rua das Estrelas, 4150–762 Porto, Portugal*
[2] *International Centre for Radio Astronomy Research, The University of Western Australia, 7 Fairway, 6009, Crawley WA, Australia*
[3] *ARC Centre of Excellence for All Sky Astrophysics in 3 Dimensions (ASTRO 3D), Australia*
[4] *Centre for Astrophysics Research, University of Hertfordshire, College Lane, Hatfield, AL10 9AB, UK*
[5] *University of Helsinki, Department of Physics, Gustaf Hallstromin katu 2 00140 Helsinki, Finland*
[6] *European Southern Observatory, Karl-Schwarzschild-str., 2, 85748 Garching, Germany*

ABSTRACT

We present HI and radio continuum, narrow–band Hα imaging, IFU spectroscopy, and X–ray observations of the FGC 1287 triplet projected $\sim$ 1.8 Mpc west of the galaxy cluster Abell 1367. One triplet member, FGC 1287, displays an exceptionally long, 250 kpc HI tail and an unperturbed stellar disk which are the typical signatures of ram pressure stripping (RPS). To generate detectable RPS signatures the presence of an Intra–cluster medium ICM/intra–group medium IGM with sufficient density to produce RPS at a realistic velocity relative to the ICM/IGM is a prerequisite. However, *XMM–Newton* observations were not able to detect X–ray emission from the triplet, implying that if a hot ICM/IGM is present, its density, n_e, is less than 2.6×10^{-5} cm^{-3}. Higher–resolution VLA HI data presented here show FGC 1287's HI disk is truncated and significantly warped whereas the HI tail is clumpy. TNG Hα imaging identified three star forming clumps projected within 20 kpc of FGC 1287's disk, with VIMOS–IFU data confirming two of these are counterparts to HI clumps in the tail. The triplet's HI kinematics, together with Hα and radio continuum imaging suggests an interaction may have enhanced star formation in FGC 1287's disk, but cannot readily account for the origin of the long HI tail. We consider several scenarios which might reconcile RPS with the non–detection of ICM/IGM X–ray emission but none of these unambiguously explains the origin of the long HI tail.

Key words: galaxies:clusters:individual: (Abell 1367) galaxies: groups: individual: FGC 1287 triplet galaxies: ISM

1 INTRODUCTION

Details of how, when and where the galaxy cluster environment impacts late–type galaxies (LTGs) infalling into clusters remains to be definitively determined. HI observations from low-z clusters ($z \lesssim 0.03$) suggest that hydrodynamic interactions with the intra–cluster medium (ICM), e.g., ram pressure stripping, viscous stripping, thermal evaporation and starvation are the dominant mechanisms removing the interstellar medium (ISM) from cluster LTGs and accelerating their evolution toward earlier morphological types (Boselli & Gavazzi 2006; Cortese et al. 2021). Hydrodynamic stripping of the ISM (primarily HI) from cluster LTGs is caused by their interaction with the ICM during their orbits through a cluster. Within a few hundred kpc of cluster cores, ICM electron number densities (n_e) are $\geqslant 10^{-3}$ cm^{-3} (Bahcall 1999) and galaxy velocities relative to the ICM (v_{rel}) can exceed $\sim$ 1000 km s^{-1}. Under these conditions ram pressure stripping, thermal evaporation and viscous stripping, collectively "RPS",

are a viable mechanism to explain most of the observed ongoing cold and ionized gas stripping signatures on time scales of a few $\times$ 10^8 yr (e.g., Gavazzi et al. 1995; Bravo-Alfaro et al. 2000; Vollmer et al. 2004; Chung et al. 2009; Yagi et al. 2017; Jáchym et al. 2019; Poggianti et al. 2019). RPS could also feasibly account for most of the observed HI deficiencies and star formation (SF) quenching in LTGs within the virial radii of nearby clusters (Solanes et al. 2001; Cortese et al. 2012). The ram pressure (P_{ram}) a cluster galaxy is subject to depends on a combination of ICM density (ρ_{ICM}) and its velocity relative to the ICM (v_{rel}), i.e., $P_{ram} = \rho_{ICM} \, v_{rel}^2$ (Gunn & Gott 1972).

One–sided tails of galaxies in clusters, consisting variously of combinations of stars, cold and ionised gas, have commonly been attributed to RPS. Figure 1 shows the projected tail length of a representative sample of 44 galaxies with one–sided RPS tails from 9 clusters, as a function of their distance from the cluster centre and normalised by cluster virial radius. Where a galaxy has a multi–phase tail, the tail length in the plot is for the phase with the largest projected length. The data for the galaxies shown in the plot is from papers by Gavazzi & Jaffe (1987); Gavazzi et al.

[*] E-mail: tom.scott@astro.up.pt (TCS)

(1995, 2001); Cortese et al. (2007); Chung et al. (2007); Yoshida et al. (2008); Hester et al. (2010); Sun et al. (2010); Scott et al. (2010, 2018); Smith et al. (2010); Yagi et al. (2010, 2017); Boselli et al. (2016); Jáchym et al. (2017, 2019); Poggianti et al. (2017, 2019); Bellhouse et al. (2019); Ramatsoku et al. (2019); Moretti et al. (2020); Müller et al. (2021). The plot includes the tails observed for the Blue Infalling Group (BIG) and FGC 1287, both in Abell 1367. All of the RPS tails, except FGC 1287, are projected within $\sim 40\%$ of their cluster's virial radius (≈ 1 Mpc) and are predominantly found in large, ICM rich clusters. In several cases, RPS appears to be aided by tidal interactions and/or AGN activity "loosening" gas from the parent galaxy's gravitational potential well (e.g., Consolandi et al. 2017; Poggianti et al. 2020). FGC 1287's uniqueness is clear from this plot both in terms of its distance from the cluster centre and the length of its tail.

Beyond the virial radii of clusters, it is less clear whether RPS significantly impacts LTGs. This is primarily because X–ray emission from the ICM has not been detected there and, while we expect that low density warm medium undetectable by X–ray telescopes should be present (Cen et al. 2001; Macquart et al. 2020), it is still debated whether hydrodynamical effects remain the dominant environmental mechanism affecting galaxy evolution in the outskirts. Indeed, many authors, e.g., Dressler (2004), argue that in these environments prolonged exposure to intra–group tidal interactions and "preprocessing" more generally, is more efficient in affecting the cold gas reservoirs of galaxies. Evidence of the impact of preprocessing on the H I in LTGs in a rich infalling group was recently presented in Kleiner et al. (2021), see also Cortese et al. (2021).

To settle this debate, further resolved H I observations of galaxy clusters are required as the H I morphology and kinematics of disturbed galaxies can provide important insights into the mechanisms at play. In this paper we extend our previous analysis of one of the most dramatic examples of a one–sided H I tail in the cluster outskirts: FGC 1287 (Scott et al. 2012). Despite being at a projected distance ~ 1.8 Mpc west of the centre of A 1367, this galaxy shows an extraordinarily long 250 kpc H I tail, significantly longer than the typical HI tails associated with RPS galaxies near the centres of clusters.

In this paper we report on high resolution NRAO[1] Karl G. Jansky Very Large Array (VLA) B– and C–configuration H I and radio continuum, ESO[2] VLT/VIMOS[3], VIsible Multi–Object Spectrograph (VIMOS) integral field unit (IFU) spectroscopy (hereafter VIMOS–IFU) and *XMM–Newton* X–ray observations of the FGC 1287 triplet. Additionally, we present narrow band Hα imaging of FGC 1287 from the Telescopio Nazionale Galileo (TNG) 3.58-m telescope located at Roque de Los Muchachos, La Palma, Spain.

Section 2 summarises the observations, with observational results in section 3. A discussion follows in section 4 with concluding comments in section 5. Based on a redshift to A 1367 of 0.022 and assuming $\Omega_M = 0.3$, $\Omega_\Lambda = 0.7$, and $H_o = 72\,\mathrm{km\,s^{-1}\,Mpc^{-1}}$ (Spergel et al. 2007) the distance to

the cluster is ~ 92 Mpc and the angular scale is $1\,\mathrm{arcmin} = 24.8\,\mathrm{kpc}$. All projected positions referred to throughout this paper are in J2000.0.

2 OBSERVATIONS

2.1 VLA

The FGC 1287 triplet was observed with the VLA in B– (9.2 hrs on source) and C– configurations (3.2 hrs) in L–band (1420 MHz; project ID:13B–019). A summary of each day's observation is set out in Table 1.

Each day's observation was configured to record 10 spectral windows (spw), 8 of which contained 64 continuum channels each at full polarisation and with the other two spws set up with 1028 channels for spectral line observations, in dual polarisation mode. Spw 3 was set up to observe the H I line of neutral atomic hydrogen and generated a position–position–velocity cube ($\alpha, \delta, velocity$) with 1028 (7.81 kHz wide) channels. The remaining spw was centred on the OH transitions which were, however, not detected and no further use was made of this spw.

Each day's measurement set was reduced with the VLA pipeline provided within the Common Astronomy Software Applications package (CASA) following standard procedures (McMullin et al. 2007). After verifying each day's observations reached the required quality and expected noise value, we combined the visibilities of the H I measurement sets (spw 3) into a single combined (B/C configuration) measurement set using the CASA task CONCAT. We removed the continuum from this combined measurement set using the task UVSUB. To further reduce the effect of RFI in this cube we inspected the continuum subtracted uv–data and flagged visibilities with amplitudes > 2.5 Jy. On this H I continuum subtracted, combined B/C configuration measurement set we used the task TCLEAN and produced a cube with with 352 channels (barycentric optical velocity range of $5953\,\mathrm{km\,s^{-1}}$ to $7708\,\mathrm{km\,s^{-1}}$) with a reduced velocity resolution of $5\,\mathrm{km\,s^{-1}}$, to increase the S/N (rms per channel of ~ 0.32 mJy). The synthesised beam for this cube was 13.84 arcsec × 12.69 arcsec, PA=178.09°. Because we were particularly interested in the faint H I emission in the FGC 1287 tail we produced the B/C configuration H I cube using natural weights. Natural weighting improves sensitivity at the cost of angular resolution. No self–calibration was required.

For the B/C configuration H I cube the 3σ detection limit in a three channel average was $\mathrm{N(HI)} = 5 \times 10^{19}\,\mathrm{atom\,cm^{-2}}$ ($2 \times 10^7\,\mathrm{M_\odot}$). A three channel average corresponds to a linewidth of $15\,\mathrm{km\,s^{-1}}$ which in turn corresponds to a velocity dispersion of $6\,\mathrm{km\,s^{-1}}$ which is what is typically found in the outskirts of disk galaxies (Tamburro et al. 2009). H I moment 0 and 1 maps (integrated H I and velocity field, respectively) were extracted from the final B/C configuration cube (velocity resolution of $5\,\mathrm{km\,s^{-1}}$) after blanking carried out in the following manner with CASA: 1) the H I cube was spatially smoothed with a boxcar 3 × 3 filter. 2) pixels in all channels beyond the previous D–configuration moment 0 3σ contour were masked (i.e., discarded). 3) all remaining pixels with fluxes below a 2σ clip were masked 4) channels with velocities where no AGES H I flux was detected in the triplet or AGES J113939+193524 were fully blanked. 5) only those

pixels were retained which formed part of coherent structures in velocity by comparing for each channel what emission was present in adjacent channels. This was done manually and had the effect of removing noise peaks that are above the 2σ clip threshold in one channel only. 6) the masks from the previous steps were combined and applied to the original unsmoothed B/C configuration cube to produce a blanked cube to which the CASA task IMOMENTS was applied to extract the moment 0 and 1 H I maps. For the 8 continuum spws we carried out additional flagging of the calibrated B and C configuration measurement sets using AOFlagger.

2.2 VIMOS–IFU

The observations were obtained using VIMOS–IFU on the 8.2 m VLT UT3/Melipal telescope in Chile. The VIMOS–IFU consists of four CCD quadrants covered by a pattern of 1600 elements. We used a projected size per element of 0.33", covering a total field of view of 13" × 13". Four VIMOS–IFU pointings were obtained on the 10th and 16th of February 2016, two at the optical centre of FGC 1287 and two at the positions of Hα emitting clumps (SFC1 and SFC2) north of the optical centre (see Figure 2). Two science exposures of 830 s were taken per pointing. A third dithered exposure of 290 s was taken, after each observation, in order to obtain a night sky background exposure.These observations used the High Resolution (HR) HR–orange grating (0.62 Å pixel^{-1}), offering a spectral resolving power R = 2650 between $\sim$ 5100–7699 Å. The data were reduced using the *esorex* software version 3.10.2. This included bias subtraction, flat–field correction, wavelength and flux calibration. The flux calibration was based on observations of spectrophotometric standard stars included in the standard VIMOS calibration plan. The 2D data images were combined into 3D data cubes and resampled to a 0.33" spatial resolution. Finally, we correct the resulting data cubes for the quadrant–to–quadrant intensity differences. We renormalized the quadrants by comparing the intensity levels of the neighbouring pixels at the quadrant borders. More details about the data reduction can be found in Lagos et al. (2016, 2018).

2.3 Hα imaging

FGC 1287 was imaged with the Device Optimized for LOw RESolution (DOLORES) attached at the Nasmyth B focus of the 3.6-m Telescopio National Galileo on 23rd February and 15th March, 2012. Narrow–band imaging was obtained using a [SII] narrow band filter centred at $\sim$6724 Å with a width of $\sim$57 Å to include the red–shifted Hα line, with the underlying continuum estimated via broadband (Gunn) r' filter observations. Total exposure time was 9600 sec and 7560 sec for the narrow and broad–band observations, respectively. Data reduction was performed using standard techniques in IRAF, following the same procedure as described in Cortese et al. (2006).That is all single science frames were stacked after individual bias subtraction and flat-fielding, using the INCOBINE and IMARIT tasks. The combined OFF–band frame was then normalised to the combined ON–band one by the flux ratio of a few foreground stars. The Hα+[NII] NET image shown in the lower right panel of Fig. 2 was then obtained by subtracting the normalized OFF–band image from the ON–band one.
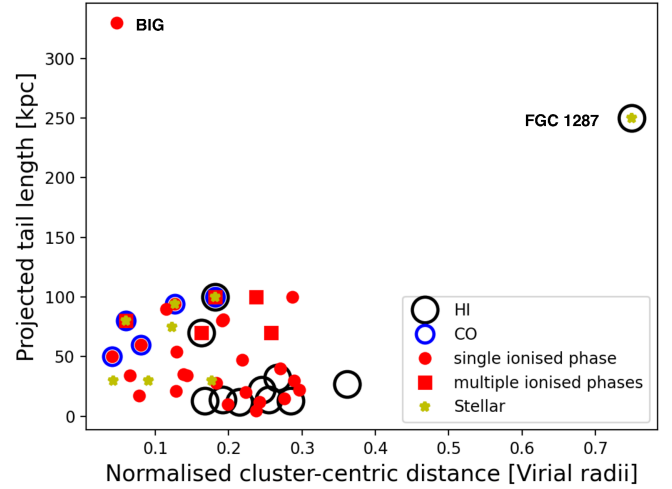

Figure 1. Cluster galaxies with one–sided tails taken from a literature sample of galaxies with one–sided tails as well as FGC 1287 and the BIG group (see main text for details). Plotted is projected tail length against distance from the cluster centre normalised by cluster virial radius. The symbols indicate the different types of tails: circles = cold gas (H I – black, CO – blue), red = single or a combination of tracers of ionised gas (Hα,UV, X–ray) and/or radio continuum), i.e. plasma tails and stars = stellar.

2.4 XMM–Newton

XMM–Newton observed FGC 1287 on 16 June 2012 for a duration of 18.4 ksec, observational ID 0690780101. The thin filter was used with all EPIC cameras, with total clean exposures of 11.0, 17.6 and 16.1 ksec for PN, MOS1 and MOS2, respectively. The observational setup used is sensitive to the X–ray emission of the gas with temperatures above 0.1 keV. Lower temperature gas in collisional ionization equilibrium would remain undetected in this experiment.

The source was not detected in the combined 0.5–2 keV band image. Using a 5 arcmin radius centred on FGC 1287, we extracted PN spectrum and adopted a 2σ limit to normalise the APEC plasma model using a temperature of 0.5 keV, leading to a corresponding limit on the gas mass of 7 × $10^9 M_\odot$, assuming a uniform gas distribution.

3 OBSERVATIONAL RESULTS

3.1 HI and Radio continuum properties

The VLA B/C–configuration H I column density (henceforth referred to as moment 0) maps for FGC 1287 and neighbouring galaxies CGCG 097-036 and CGCG 097-041 reveal an H I tail clumpier than originally suggested by the lower resolution VLA—D configuration observations presented in Scott et al. (2012). Figure 2 shows at least five separate structures above an H I column density of $\sim$3.1 × 10^{20} atoms cm^{-2} are visible within the H I tail (labeled SFC1, SFC2, SFC3, CLP4 and CLP5). H I was also detected in AGES J113939+193524 (Cortese et al. 2008), which is the H I counterpart of the optical dwarf galaxy SDSS J113939.67+193516.7, see Appendix A. Properties of the VLA H I detections are summarised in Tables 2 and 3. As a check we also applied the SOFIA–2

Table 1. VLA observational parameters

Date	Configuration	Pointing centre α_{2000} [^{h} ^{m} ^{s}]	δ_{2000} [$^\circ$ $'$ $''$]	Int.[a] time [hours]	Central[b] Velocity [km s^{-1}]
14 Nov 2013	B	11 39 08.3	19 39 02.2	2.3	6830
15 Nov 2013	B	11 39 08.3	19 39 02.2	2.3	6830
24 Nov 2013	B	11 39 08.3	19 39 02.2	2.3	6830
30 Nov 2013	B	11 39 08.3	19 39 02.2	2.3	6830
6 Dec 2014	C	11 39 08.3	19 39 02.2	3.2	6830

[a] On target integration time.
[b] Barycentric optical velocity of the H I spectral window.

(Serra et al. 2015) source finding code to the unmasked B/C configuration H I cube which generated moment maps in good agreement with those produced with our manual blanking procedure (Section 2.1), recovering all five H I tail clumps with ⩾ 90% reliability.

The velocity field for the FGC 1287 group is shown in Figure 3, with a zoom–in of the H I moment 0 map and velocity field for each group member shown in Figure 4. Whereas the SW side of the FGC 1287 disk shows a regular rotation pattern in the velocity field, the NE part reveals a rapidly changing position angle (PA), between ∼ 6850 km s^{-1} to 6900 km s^{-1}, and closed iso–velocity contours indicating a serious warp. This feature is also seen in the D–configuration H I velocity field. The lower panel of Figure 5 presents the spatially integrated H I profile for the FGC 1287 disk extracted from the VLA B/C–configuration cube. This displays the double horn profile expected from an edge–on rotating disk. Kinematic modelling of the H I disk, e.g., with ^{3D}BAROLO (Di Teodoro & Fraternali 2015), was not carried out because the small number of beams across the FGC 1287 H I disk and the evidence of an asymmetric warp from the H I velocity field made it clear that any model fit obtained would be highly uncertain. Another kinematic feature is a sequential increase in the velocity of the principal H I clumps in the tail with increasing distance from optical disk, see Table 4. The clump velocities fall within ± 75 km s^{-1} of the systemic velocity of the FGC 1287 disk, i.e., the radial velocities of the tail clumps are closer to the V$_{HI}$ of FGC 1287 and the other two triplet members than velocities at the edge of the H I disk. The dashed vertical lines in Figure 5 correspond to the optical velocities of CGCG 097-036 and CGCG 097-041.

In the upper panel of Figure 5 we compare the integrated H I profiles for the FGC 1287 disk + tail from the VLA B/C– and VLA D–configurations as well as from a new extended AGES survey (Deshev et al. 2022 in prep.), referred from here on as AGES. The VLA–D configuration has a 3σ H I column density detection limit of ∼ 2×10^{19} atoms cm^{-2} (Scott et al. 2012). From the figure it is clear that the VLA configurations, and particular the B/C configuration, are missing substantial fractions of H I flux. In the case of the B/C array this is due to a combination of a lack of short spacings and the lower H I column density detection limit. For the D–configuration the integration was relatively short (2.3 hrs) and the difference between its spectrum and AGES is primarily attributable to the difference in column density sensitivity (see below) as there should not have been any issue with detecting extended emission at scales of several arcmin as such.

To gain a more complete understanding of the H I in the triplet, bearing in mind the VLA flux losses relative to AGES, we made a comparison (at common spatial and velocity resolution) between H I cubes containing the triplet and the H I tail from AGES and the VLA B/C– and D–configuration. More specifically we compared the H I detected in a region within the 3σ H I contour in the AGES integrated H I map of FGC 1287 and the tail, and compared this with the two VLA data cubes. This comparison revealed a substantial mass of low column density H I to the east of the FGC 1287 VLA–D H I disk and in the H I tail. The additional diffuse H I detected in AGES in these regions was below the VLA–D detection limit (∼ 2×10^{19} atom cm^{-2} but above the AGES 3σ limit of ∼ 4.5×10^{17} atom cm^{-2} (Keenan et al. 2016). For FGC 1287 (disk + tail) the mass of this low column density H I was estimated at ∼ 5×10^9 M$_\odot$. The highest concentration of this low column density H I lies to the east of the FGC 1287 at about the same velocity (∼ 6800 km s^{-1}), as the mean optical velocity of the triplet (6804 km s^{-1}) Our analysis indicates the VLA–D, and particularly VLA–B/C configurations, are only tracing the highest column density H I within a more extensive distribution of diffuse H I revealed by AGES.

Using the VLA D–configuration we find a total H I mass of the FGC 1287 disk + tail of 9.4×10^9 M$_\odot$. Following (Scott et al. 2010) we determined the H I deficiency for FGC 1287 disk + tail by comparing this with the expected H I content of similar, isolated galaxies of the same optical size and morphological type and find an H I deficiency of -0.27, i.e., an excess. If we rather use the H I mass (1.3×10^{10} M$_\odot$) based on the more sensitive AGES survey the H I excess rises to -0.42. Whereas an H I deficiency of -0.27 is within the range expected for gas–rich galaxies, an H I deficiency of -0.42 indicates either the galaxy was particularly H I–rich before producing the tail or, more likely, a significant fraction of the H I in the tail did not originate from FGC 1287 but is possibly from another triplet member and/or an H I rich dwarf. Although we note the metallicity of SFC1 (see next section) is inconsistent with dwarfs as a source of its H I, this does not preclude them as a source of H I in other parts of the tail.

Figure 6, shows 1.4 GHz radio continuum (RC) was detected in the disk of FGC 1287 using the VLA in B–configuration (5.4×4.9 arcsec beam). The FGC 1287 1.4 GHz RC, TNG Hα+[NII] (Figure 7) and the nominally 145 MHz RC image (not shown) obtained with LOFAR (Bempong–Manful et al. in prep) all show quite similar morphologies. In Figure 6 the 1.4 GHz RC contours display asymmetric features extending ∼ 10 arcsec (4 kpc) both north and south

of the FGC 1287 disk centre, features slightly more prominent on the north side of the object, with LOFAR confirming this morphology. Similar extra–planar features are seen in the Hα+[NII] (Figure 7). We tried to look for differences in the spectral slope in the 1.4 GHz RC in the FGC 1287 extra–planar regions which might have confirmed outflows but the signal to noise in these regions was too low to carry out such an analysis. Two further features were found to be common to the Hα+[NII] and the two RC maps. First, the morphologies are asymmetrically distributed along the optical disk favouring the SE, with the NE end of the each disk, where the H I kinematic warp is located, being truncated relative to the optical disk (see Figure 7). Second, there is no evidence of upstream compression of the emission contours that you would expect from RPS.

We use the RC luminosity to estimate the current star formation rate (SFR) for FGC 1287 following Equation 3 from Heesen et al. (2014), with an inclination correction, finding a value of $\sim 3.2 \, \mathrm{M_\odot \, yr^{-1}}$ (see also Table 2). This is a factor of ~ 3 higher than is observed in star–forming main sequence galaxies in the Local Volume with the same stellar mass (e.g., $0.811 \, \mathrm{M_\odot \, yr^{-1}}$ Speagle et al. 2014), suggesting that the environmental process responsible for the H I tail has not reduced SFR of FGC 1287 but might have recently enhanced it.

3.2 Ionised gas properties

As noted in Section 3.1 we identify 5 distinct H I clumps in the tail. The first three as one moves northwards along the H I tail (SFC1, SFC2 and SFC3) coincide with blue stellar continuum emission in optical imaging available as part of the DECam Legacy Survey (DECaLS), (Blum et al. 2016), lower left panel of Figure 2 (DECaLS imaging is deeper than SDSS). These three clumps are also seen as star forming Hα emitting clumps in the TNG narrow-band Hα+[NII] image in the lower right panel of Figure 2. Two H I clumps further north along the tail (CLP4 and CLP5) are not associated with any obvious SF activity. In Figure 2 – lower left panel, the small blue galaxy just above the SW edge of FGC 1287 is ASK 626970 which is projected in the foreground of the triplet with an optical velocity of 1733±2 km s^{-1} (SDSS).

The star forming nature of SFC1 and SFC2 could be confirmed by our VIMOS–IFU observations as they detect clear Hα emission coming from both clumps. The spectra for both clumps, as well as Hα maps and velocity fields are shown in Figure 8. These were obtained by fitting emission line fluxes (Hα and [NII]λ6584) with a single Gaussian profile. The velocity field for SFC1 and SFC 2 suggests the presence of a velocity gradient. The velocity field of the central part of FGC 1287, basically covering the VLA B/C–configuration synthesised beam central pointing on the galaxy, shows emission from a disk in regular rotation.

The derived log([NII]λ6584/Hα) line ratios are -0.62±0.08 and -0.25±0.09 for SFC 1 and the central FGC 1287 disk, respectively. These confirm that, in both cases, ionisation comes mainly from young stars. We can thus use the Denicolo calibrator (Denicoló et al. 2002) to derive an estimate of the oxygen abundance for both objects, finding 8.67± 0.12 and 8.94± 0.09 for SFC1 and FGC 1287, respectively. This indicates that the gas in SFC1 was pre–enriched and most likely has its origin in the triplet and is not infalling, primordial material.

We used the relationship given in Kennicutt (1998) to estimate the star–formation rate, SFR(Hα), for SFC1, SFC2 and the portion of the FGC 1287 disk within the VIMOS field of view (FoV), after correction for galactic extinction. No correction for internal extinction was possible as the spectrum did not cover the Hβ line. In Table 4 we show the radial velocity $V_{H\alpha}$, Flux(Hα), Flux([NII]), 12+log(O/H) and SFR(Hα) for the central FGC 1287 disk, SFC1 and SFC2, respectively.

3.3 XMM–Newton

No X–ray emission was detected in the combined 0.5 to 2 keV band *XMM–Newton* image using a 5 arcmin radius centred on FGC 1287. We extracted a PN spectrum and set the 2σ limit on the normalisation of the APEC plasma model using a temperature of 0.5 keV, with a corresponding limit on the gas mass of $7 \times 10^9 \, \mathrm{M_\odot}$, assuming a uniform gas distribution. This non–detection of hot X–ray emitting IGM/ICM implies an upper limit of $n_e < 2.6 \times 10^{-5} \, \mathrm{cm^{-3}}$ within a 5 arcmin radius, which falls two orders of magnitude below the densities in the X-ray detected ICM of Virgo, Coma, or A 1367 (Boselli et al. 2006). Having said that, we would not have been able to detect any warm intergalactic medium (WHIM) filaments with temperatures $\sim 10^6$ K and densities $\sim 10^{-4} \, \mathrm{cm^{-3}}$ that are predicted beyond the virial radius in some cluster simulations (Cen et al. 2001, see also Cortese et al. (2021)). However, more typically such filaments are expected to have densities of $\sim 10^{-6} \, \mathrm{cm^{-3}}$.

We used the β model, parameters in Ge et al. (2021) for the A 1367 NW and SE subclusters applying them to the Cavaliere & Fusco-Femiano (1976); Gorenstein et al. (1978) ICM density profile model, (Reynolds et al. 2021, equation 10). This gave ICM densities at the position of FGC 1287 of $n_e = 1.5 \times 10^{-5} \, \mathrm{cm^{-3}}$ for the NW subcluster and $n_e = 3.1 \times 10^{-5} \, \mathrm{cm^{-3}}$ for the SE subcluster. In principal the sum of these densities ($n_e = 4.6 \times 10^{-5} \, \mathrm{cm^{-3}}$) provides an estimate of the ICM density at the position of FGC 1287, but the merging of the two subclusters means this prediction is more uncertain than for dynamically relaxed clusters. However, the XMM ICM density upper limit is consistent to a first order with the β model densities. Although, we note that using a sample of 39 galaxy clusters observed in X–ray (*ROSAT*) Vikhlinin et al. (1999) found a steepening of the density profile beyond 0.3 virial radii.

4 DISCUSSION

4.1 Nature of the triplet

Scott et al. (2012) showed that FGC 1287, together with CGCG 097-41 and CGCG 097-36 are projected ~ 1.8 Mpc west of the A 1367 cluster centre and between the cluster's r_{200} and r_{vir}. This means they are projected within the cluster's 2.58 Mpc r_{vir} (Moss 2006) and their mean optical velocity is only 313 km s^{-1} greater than the cluster's velocity (Cortese et al. 2004). Given the three galaxies are projected well within the clusters virial radius and the cluster's velocity dispersion of 891 km s^{-1} (Cortese et al. 2004) it is a reasonable assumption that they are bound to the cluster and have begun falling toward it, either individually or as a group. All three galaxies fall within a projected diameter of 200 kpc,
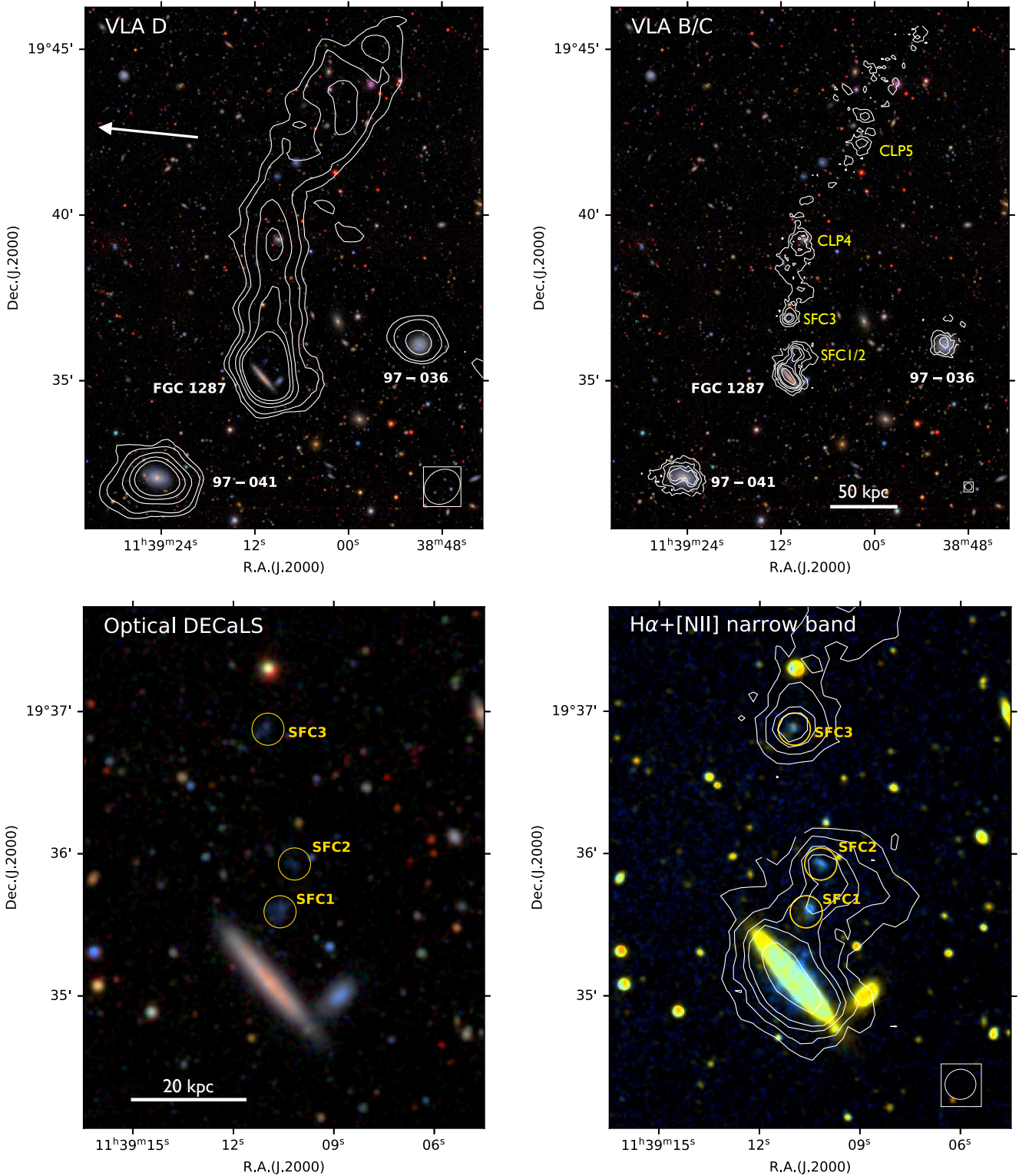
Figure 2. FGC 1287 group: (*top left:*) H I VLA D–configuration H I column density map as contours on an SDSS g, r, i–band image, coded as BGR (Scott et al. 2012). Contours are at 1.6, 2.6, 5.2, 7.8 and 10.3×10^{19} atoms cm^{-2}. The boxed ellipse in the lower right shows the size ($72'' \times 60''$) and orientation of the VLA D–configuration synthesised beam. The arrow points in the direction of the A 1367 cluster centre. (*top right:*) H I VLA B/C–configuration H I column density map as contours on an SDSS g, r, i–band image, coded as BGR. H I contours are at column densities of 0.5, 1.6, 3.1, 4.7, 6.2, 9.3, and 12.5×10^{20} atom cm^{-2}. The three H I detected galaxies are marked together with the projected positions of principal H I clumps in the FGC 1287 tail. (*bottom left:*) Optical g, r, z DECaLS image of the region at the base of the FGC 1287 H I tail. The small blue galaxy just above the SW edge of FGC 1287 is ASK 626970 which is projected in the foreground of the triplet. (*bottom right:*) TNG Hα+[NII] narrow band image (blue) of the the region at the base of the FGC 1287 H I tail overlaid with VLA B/C–configuration H I contours (contour levels as per top right panel. The beam size and orientation of VLA B/C–configuration synthesised beam is indicated by the boxed ellipse at the bottom right and measures $13.8'' \times 12.7''$).

Table 2. H I, radio continuum and optical properties of the VLA H I detections.

Galaxy ID	RA [^{h} ^{m} ^{s}]	DEC [$^\circ$ $'$ $''$]	V_{HI}[a] VLA–B/C [km s^{-1}]	W_{20}[b] VLA–B/C [km s^{-1}]	SFR(RC) VLA-B [M$_\odot$ yr^{-1}]	M$_*$ [10^9M$_\odot$]	Dist. from FGC1287 [kpc]
FGC 1287 –disk			6788±3	335±5	3.2	8.59	–
FGC 1287–tail			6818±11	185±22	–	–	–
FGC 1287–all	11 39 10.9	+19 35 06	6803±26	285±52	3.2	8.59	–
CGCG 097-036	11 38 51.0	+19 36 05	6808±14	75±28	1.7	9.91	119
CGCG 097-041	11 39 24.4	+19 32 05	6786±5	260±10	1.5	33.26	109
SDSS dwarf[c]	11 39 39.7	+19 35 17	7381±4	60±7	–	0.002	167

[a] Barycentric optical V_{HI} calculated using the method described in Scott et al. (2010).
[b] W_{20} calculated using the method described in Scott et al. (2010).
[c] SDSS J113939.67+193516.7.

Table 3. H I properties of the VLA H I detections.

Galaxy ID	M(HI)[a] VLA–B/C [10^9M$_\odot$]	M(HI)[b] VLA-D [10^9M$_\odot$]	MHI(HI)[c] AGES [10^9M$_\odot$]	Def. H I[d]	A_{flux}[e]
FGC 1287 –disk	1.43	–	–	–	1.16±0.04
FGC 1287–tail	2.65	–	–	–	–
FGC 1287–all	4.08	9.4	13.0	-0.27	–
CGCG 097-036	0.34	0.8	1.98	0.14	1.07±0.05
CGCG 097-041	1.23	2.8	3.68	0.01	1.01±0.02
SDSS dwarf[f]	0.52	–	0.67	-0.27	1.26±0.05

[a] $M(\text{HI}) = 2.36 \times 10^2$ D^2 S$_{HI}$ where $M(\text{HI})$ is in M$_\odot$, D = distance (92 Mpc) and S$_{HI}$ is the VLA B/C configuration flux in Jy km s^{-1}.
[b] From Scott et al. (2012).
[c] Total HI flux from AGES applied using the formula in note a above. For FGC 1287 the H I flux for the tail+disk was extracted from the AGES cube. It should be noted this AGES H I total flux value is likely to include some side–lobe contamination from other triplet members.
[d] H I deficiencies are calculated using the method as described in (Scott et al. 2010) and using the H I fluxes from AGES, except for FGC 1287 (tail+disk) which is from the VLA D–configuration (Scott et al. 2012).
[e] A_{flux} was measured from the H I spectra as follows: FGC 1287 disk and SDSS dwarf from VLA B/C, CGCG 097-036 and CGCG 097-041 from AGES.
[f] SDSS J113939.67+193516.7.

Table 4. FGC 1287 Hα (VIMOS–IFU) and H I (VLA B/C configuration) component properties

Object	RA [^{h} ^{m} ^{s}]	DEC [$^\circ$ $'$ $''$]	V_{Ha} [km s^{-1}]	Flux(Hα) [$\times 10^{-16}$] [erg cm^{-2} s^{-1}]	Flux([NII]) [$\times 10^{-16}$] [erg cm^{-2} s^{-1}]	12+log (O/H)[c]	SFR(Hα)[a] [M$_\odot$ yr^{-1}]	V_{HI} [km s^{-1}]	W_{20} [km s^{-1}]	Dist.[b] [kpc]
disk[d]	11 39 11.13	+19 35 07.2	6827.3	131.8±6.19	73.84±3.45	8.94±0.09	0.1105±0.0052	6788	335	–
SFC 1	11 39 10.53	+19 35 36.7	6774.3	2.65±0.12	0.64±0.13	8.67±0.12	0.0022±0.0001	6728±2	35±4	13
SFC 2	11 39 10.16	+19 35 55.7	6767.9	2.15±0.10	–	–	0.0018±0.0001	6744±1	25±3	21
SFC 3	11 39 10.96	+19 36 52.2	–	–	–	– –	–	6796±2	30±5	73
CLP 4	11 39 9.36	+19 39 7.2	–	–	–	– –	–	6828±5	65±11	100
CLP 5	11 39 1.57	+19 42 32.2	–	–	–	– –	–	6863±2	35±4	184

[a] Corrected for galactic extinction.
[b] Projected distance from the optical centre of FGC 1287.
[c] Oxygen abundance using the Denicoló et al. (2002) method.
[d] FGC 1287 disk only; Hα values and metallicty are from the inner part of the disk, i.e., from within the VIMOS–IFU 13$''$ FoV.
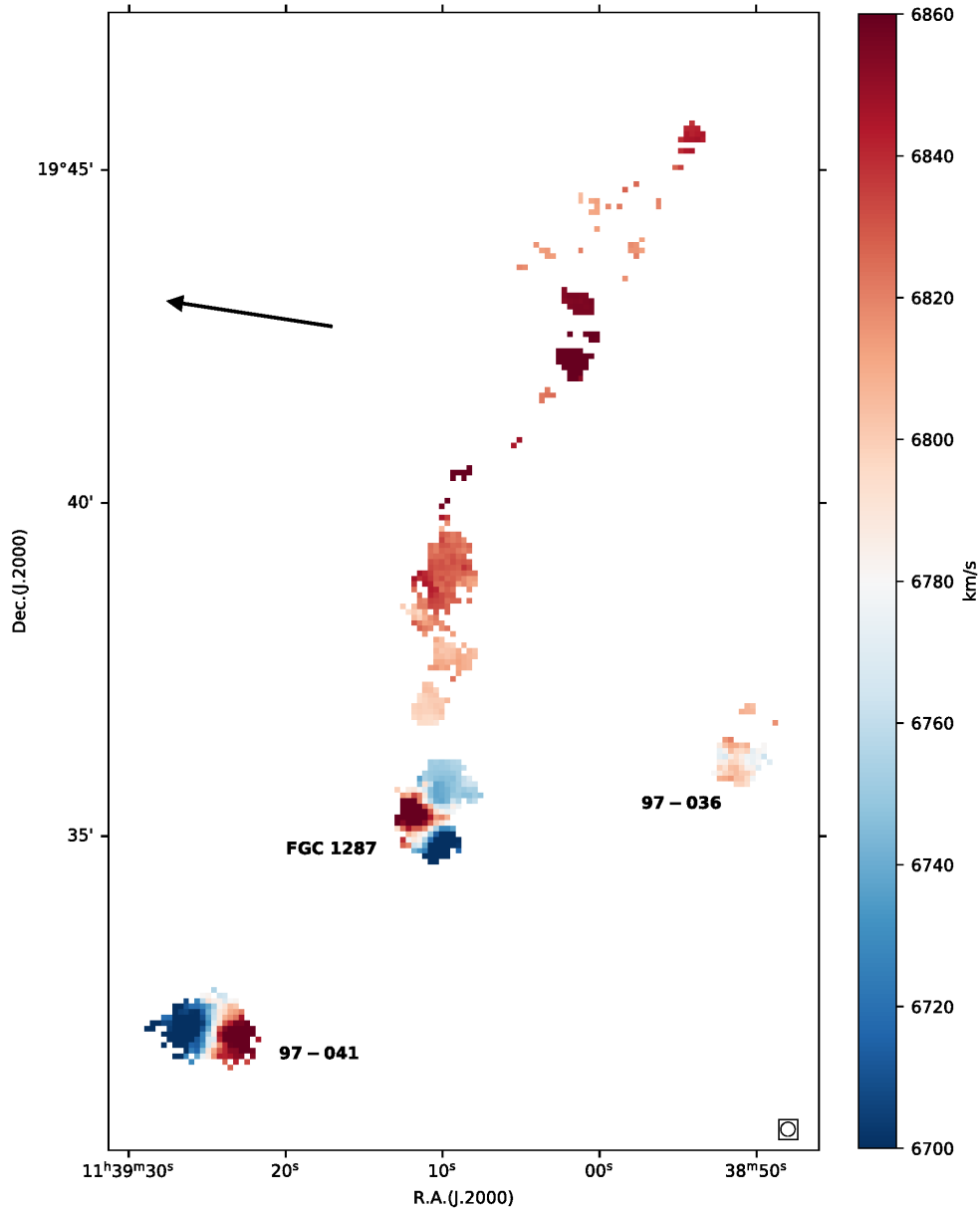
Figure 3. FGC 1287 group: H I velocity field, with velocities corresponding to the colours in the sidebar. The beam size and orientation of VLA B/C–configuration synthesised beam is indicated by the boxed ellipse in the bottom right and measures $13.8'' \times 12.7''$. The arrow points in the direction of the cluster centre of A 1367.

with the distance between FGC 1287 and each its companions ~ 100 kpc or about twice the distance from us to the Magellanic Clouds, and within a 47 km s^{-1} radial velocity range. The SDSS group catalogue by Tempel et al. (2012) only includes CGCG 097-41 as a member of a pair with FGC 1287.

To first order the optical DECaLS DR 5 images for FGC 1287, CGCG 097-036 and CGCG 097-041 present symmetric morphologies which rules out recent ($\lesssim 1$ Gyr) strong tidal interactions. However, all three galaxies display second order asymmetries which could be either intrinsic characteristics or signatures of earlier major or recent minor interactions, e.g., FGC 1287's high–intensity g–band morphology is more variable in the NW of the disk compared to the SW

consistent with the disturbance suggested by the H I velocity field.

The transverse velocities of the three galaxies are not directly constrained by our observations. However, assuming the tail originated from FGC 1287, the geometry of the H I tail suggests a transverse motion for FGC 1287 in the N–S direction, with a relatively low velocity in the E–W direction. Although the H I tail appears in the VLA moment 0 maps to belong to FGC 1287, we consider two possible origins for the tail. If the long H I tail consists of H I stripped directly from the FGC 1287 disk by RPS, referred to from here on the direct stripping scenario, it implies FGC 1287 is an interloper relative to the other two galaxies with a large N–S transverse velocity. On the other hand, the tail could consist
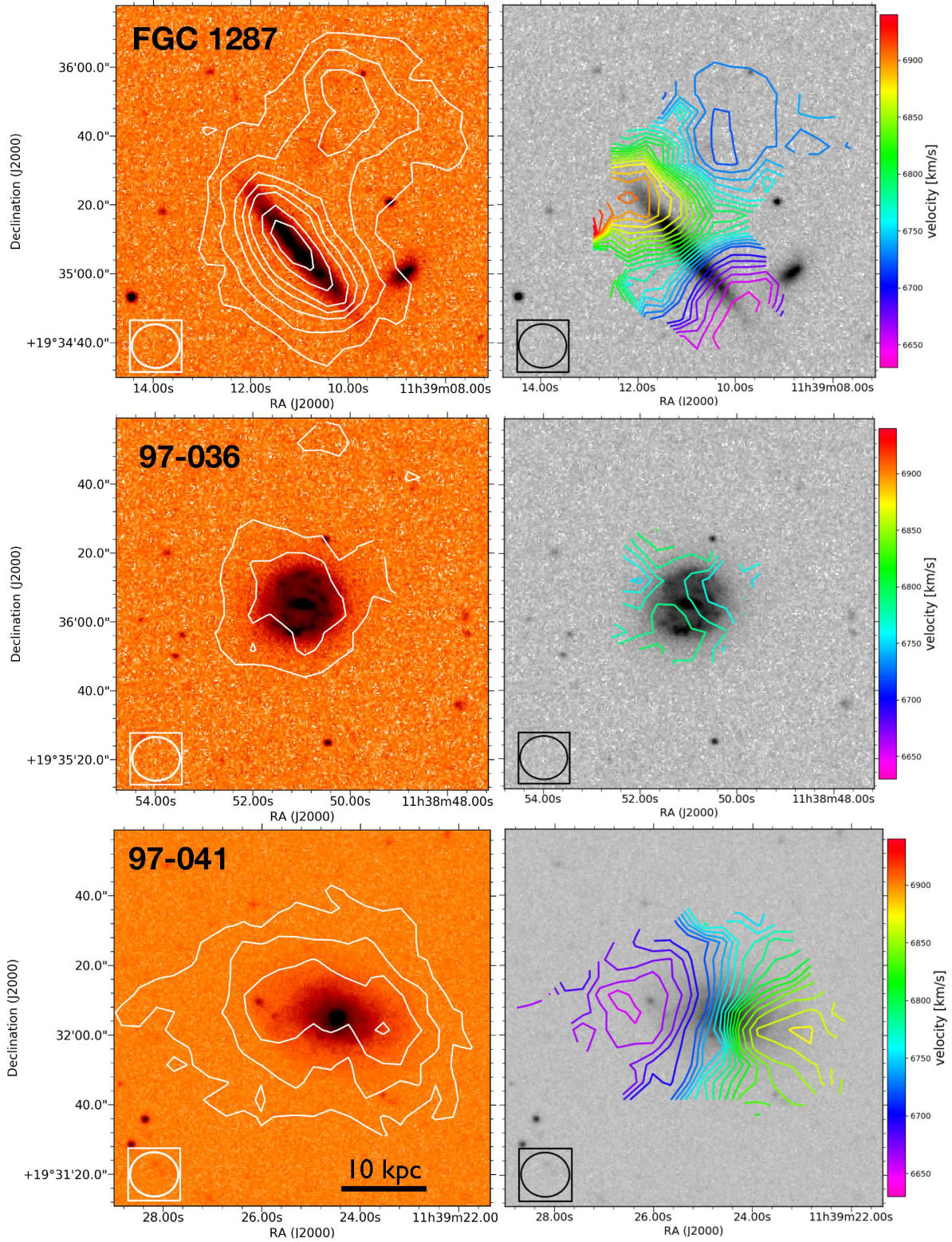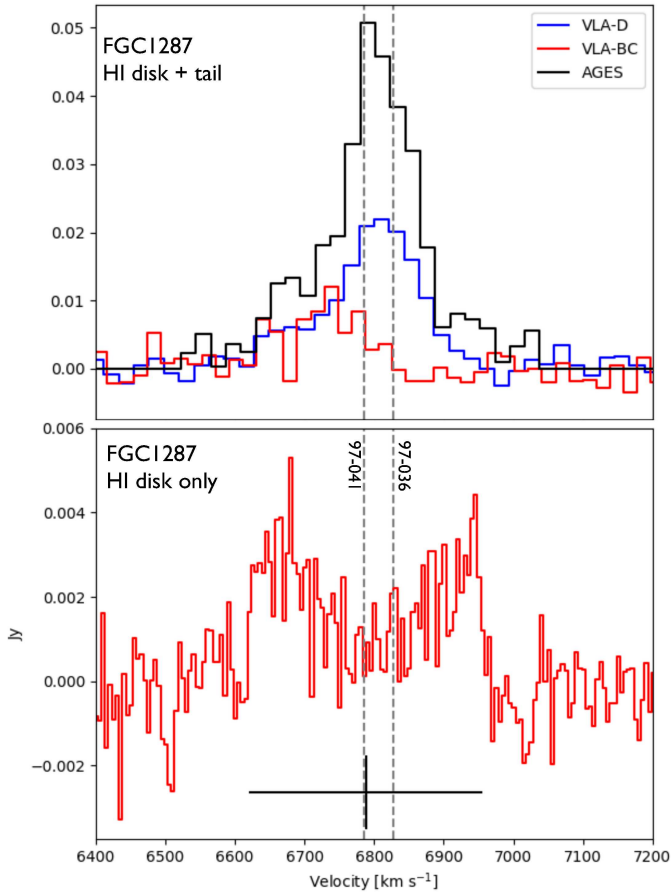
Figure 4. Galaxies in the FGC 1287 group: (*left column*) H I column density as white contours from the VLA B/C-configuration for FGC 1287, CGCG 097-036, and CGCG 097-41. The contours are at H I column densities of 0.5, 1.6, 3.1, 4.7, 6.2, 9.3, and 12.5 × 10^{20} atom cm^{-2}, i.e., the same as in Figure 2. (*right column*) H I velocity fields with contours separated by 10 km s^{-1}, except for CGCG 097-36 where the separation is 20 km s^{-1}. The background images are from the SDSS *g*–band. The beam size and orientation of VLA B/C–configuration synthesised beam is indicated by the boxed ellipse in the bottom right and measures $13.8'' \times 12.7''$).

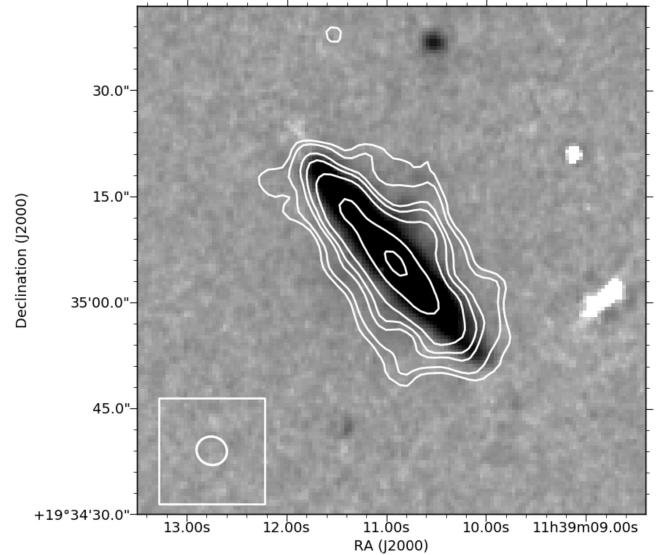**Figure 6.** FGC 1287: VLA B–configuration 1.4 GHz radio continuum contours overlaid on a smoothed TNG Hα+[NII] image with the lowest 3 σ contour at 19 μJy/beam. The boxed ellipse at the bottom left shows the size of the B–configuration $5.4'' \times 4.9''$ VLA synthesised beam and its orientation.

Figure 5. FGC 1287 *top panel:* comparison between the H I spectra for the FGC 1287 disk + tail from the AGES as well as the VLA D– and VLA B/C–configurations per the legend. The channel width of each spectrum is $21\,\mathrm{km\,s^{-1}}$. The spectra show the substantial flux loss due to the lower column density sensitivity of the VLA observations and lack of short spacings. **Lower panel:** H I spectrum for the FGC 1287 disk component extracted from the VLA B/C–configuration cube. The cross at the base of that spectrum indicates the disk component's H I W_{20} and V_{HI}. Vertical dashed lines indicate the optical velocities of CGCG 097-036 and CGCG 097-041.

of triplet cold IGM previously tidally stripped during interactions between its members and recently removed by RPS and this is referred to from here on as the combined gravitational and hydrodynamic scenario. Under either scenario the motion generating the tail appears to be principally perpendicular to radius vector pointing toward the cluster centre (see arrow in Figures 2, top left panel and 3).

The 12+log(O/H) oxygen abundance from our VIMOS–IFU analysis for SFC 1 is 8.67±0.12 and 8.94±0.09 for the central 27 arcsec² of the FGC 1287 disk. Additionally, we derived 12+log(O/H) for the inner 3 arcsec diameter of the disk from SDSS spectra for FGC 1287, CGCG 097-036 and CGCG 097-041 of 8.81 ± 0.08, 9.06 and 8.79 respectively. Whereas the VIMOS 12+log(O/H) abundance for the FGC 1287 central disk is, within the errors, higher than in

SFC 1, the uncertainties due to the limited disk areas sampled mean we are not able to distinguish SFC1's metallicity from that of any of the group members, i.e., the presence of pre–enriched material in SFC1 is expected under either RPS scenario. In the following two subsections we consider the evidence for and against the each of these RPS scenarios.

4.2 FGC 1287 direct RPS scenario

The long, narrow H I tail emanating from FGC 1287 in the VLA moment 0 maps is consistent with a morphology predicted in simulations for strong ram pressure stripping, ICM $n_e = \sim 10^{-3}\,\mathrm{cm^{-3}}$ and v_{rel} 1000 km s^{-1} near a cluster centre (Lee et al. 2020). Given the *XMM–Newton* results indicate a significantly lower ICM density ($n_e < 2.6 \times 10^{-5}\,\mathrm{cm^{-3}}$), it follows if RPS produced the FGC 1287 H I tail, it must have involved either an unusually high v_{rel} or an extremely weak gravitational restoring force binding the H I to the galaxy compared with the parameters in the simulations by Lee et al. (2020). The dynamical mass (M_{dym}) within the H I disk radius is $\sim 8.8 \times 10^{10}$ M$_\odot$ and being within the canonical range for a late–type spiral galaxy, does not suggest abnormally weak gravitational restoring forces in the FGC 1287 disk.

RPS models (e.g., Roediger & Brüggen 2007) predict outside–in truncation of H I disks. Under the direct stripping scenario the H I now in FGC 1287's tail was orginally part of its H I disk. The VLA–D configuration disk+tail M(HI) $= 9.4 \times 10^9$ M$_\odot$ (Scott et al. 2012) which provides an estimate of the FGC 1287 disk's M(HI) pior to RPS. Using this H I mass, the expected H I disk diameter, D_{HI}, $= 56\pm1$ kpc based on the D_{HI}/M_{HI} relation from Wang et al. (2016).
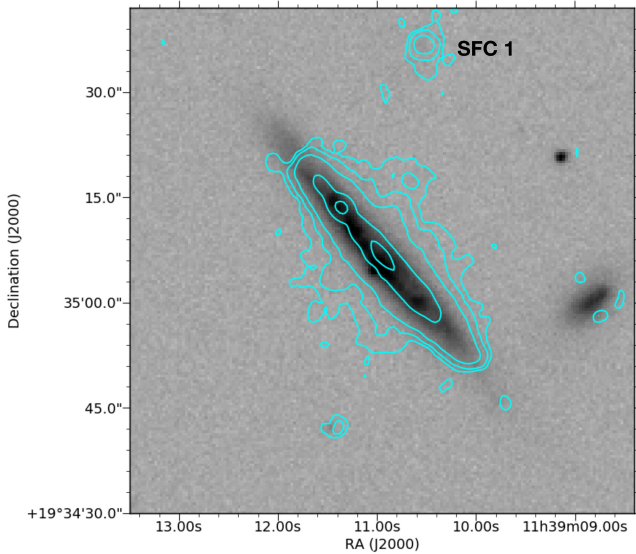
Figure 7. FGC 1287: TNG Hα+[NII] contours (3 × 3 boxcar smoothed) overlaid on an SDSS *i*–band image. The lowest contour is at ~ 3σ. The location of Hα clump SFC 1 is indicated in the figure.

FGC 1287's current H I disk diameter[4] is 1.02±0.23 arcmin (25.3±6 kpc) indicating that its H I disk is significantly truncated. Confirmation of the truncation of the FGC 1287 H I disk is seen in Figure 4 where the lowest H I column density contour approximately coincides with the optical disk edges.

An alternative way to evaluate the direct stripping scenario of the FGC 1287 H I disk is to look at the combination of velocity and ICM n_e required to truncate the FGC 1287 H I disk to its observed radius, given the upper limit for ICM n_e from *XMM–Newton*. Figure 9 shows as vertical lines the optical r_{25}, the observed H I radius and the expected H I radius, quantified above. The plot's blue curve shows the H I stripping radius using Equation 8 from Steinhauser et al. (2016) for v_{rel} with the upper limit from *XMM–Newton* for ICM n_e = 2.6 × 10^{-5} cm^{-3}. The plot shows a v_{rel} of ~ 700 km s^{-1} is required to explain the H I disk truncation at the *XMM–Newton* ICM n_e upper limit in terms of the direct stripping scenario. However the substantial mass of low column density H I, below the VLA–D detection limit and to the East of FGC 1287's disk is inconsistent with the truncated disk and narrow tail morphology expected from RPS models, at least with a v_{rel} of this magnitude.

A major difficulty for this scenario is explaining how FGC 1287 acquired a v_{rel} of ≳ 700 km s^{-1}, in such a low galaxy density environment. This v_{rel} is a factor of ≳3 higher than expected in groups and filaments. Moreover, if this v_{rel} ICM n_e combination is capable of displacing >50% of an LTGs H I mass, it is hard to understand why LTGs closer to the cluster core still contain significant H I masses This is because RPS is expected to be much more effective closer to the

cluster due to both higher ICM n_e and v_{rel} consistent with the cluster's velocity dispersion of 891 km s^{-1}.

Another possible explanation for the H I tail is that it was caused by a cluster merger shock compressing the ICM downstream of the tail. There is no indication of synchrotron emission from such a shock within a 30 arcmin radius (~ 745 kpc at the distance of A 1367) of FGC 1287 in the LOFAR image. Moreover, the orientation of the H I tail is perpendicular, rather than parallel, to the direction in which such a shock would be expected to propagate, i.e., outward from the cluster centre.

4.3 Combined gravitational and hydrodynamic stripping scenario

Under the combined gravitational and hydrodynamic stripping scenario the weakly bound cold IGM, principally H I, accumulated from multiple past intra–group interactions has recently been subject to RPS as the group fell towards A 1367 and came into contact with that cluster's warm ICM. This scenario requires a much lower v_{rel}, at the same ICM n_e, to remove H I compared to the direct stripping scenario. This is because the IGM is only loosely bound to the gravitation potential of the group compared to the more tightly bound ISM in galaxy disks. The presence of a large mass of low column density H I, below the VLA detection limit, at velocities close to the mean optical velocity of the triplet and near the projected centre of mass of the triplet is consistent with this scenario. In this scenario the H I tail would be analogous to the 330 kpc ionised Hα tail of presumably IGM material emanating from the Blue Infalling Group (BIG) in A 1367 (Yagi et al. 2017). For this scenario it is assumed that the triplet, possibly including SDSS J113939.67+193516.7, is a bound group.

FGC 1287 is a highly inclined galaxy and support for the combined gravitational and hydrodynamic stripping scenario comes from the unusual AGES and VLA–D configuration H I profiles for the FGC 1287 disk+tail in Figure 5. H I–rich high inclination LTGs typically present double horn H I profiles because of their rotating H I disks. Two high inclination A 1367 LTGs (CGCG 097-087 and CGCG 097-121) projected within 550 kpc of the cluster centre and undergoing RPS both display one–sided tails in resolved H I maps. Figure B1 in Appendix B, shows the AGES H I profiles for these high inclination galaxies displaying double horned H I profiles, with the principal H I profile asymmetry consisting of one horn being significantly smaller than the other, i.e., ram pressure is preferentially impacting the outer H I disks. Although the AGES FGC 1287 disk+tail spectrum does have secondary maxima which align with the double horns of the FGC 1287 H I disk, see Figure 5, these are dwarfed by the central maximum which is close to the FGC 1287 H I systemic velocity and the optical velocities of the CGCG 097-036 and CGCG 097-041 companions. Moreover, the D–configuration H I maxima align in velocity with the velocities of the H I clumps in the tail, rather than the velocities at the edges of the remaining truncated FGC 1287 H I disk, as would be expected from direct RPS. So, past interactions between triplet members followed by IGM RPS stripping could explain the AGES and VLA D–configuration profiles and tail clump velocities.
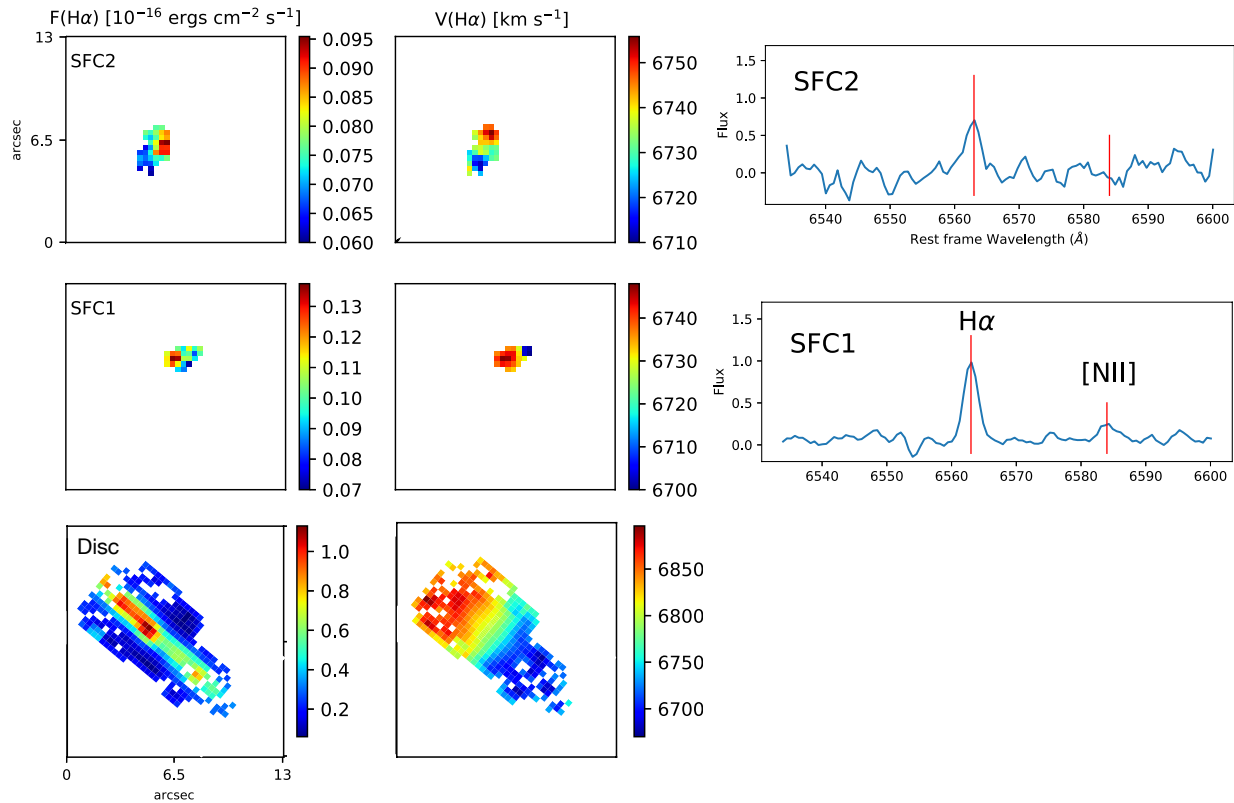
---

[4] at the 1.25×10^{20} atoms cm^{-2} contour level which is equivalent to $\Sigma_{HI} = 1\,M_\odot\,pc^{-2}$.

Figure 8. VIMOS–IFU observations of SFC1 SFC2, and the central disk of FGC 1287: *left* Flux F(Hα) in units of 10^{-16} ergs cm^{-2} s^{-1}; *middle* velocity fields V(Hα) in units of km s^{-1}; *right* VIMOS–IFU spectra at rest frame wavelengths. Flux is in units of 10^{-16} ergs cm^{-2} s^{-1} Å^{-1}. The red vertical lines indicate the rest frame wavelengths of the Hα λ 6563 and [NII] λ6584 emission lines.

4.4 Filament transit

FGC 1287 is projected $\sim$ 30 arcmin (740 kpc) south of a filament of galaxies joining the cluster from the NW (see Figure 8 in Scott et al. (2018)). So, ram pressure stripping during a N to S passage of a gas filament associated with this galaxy filament is a possible mechanism for generating the H I tail. To produce an H I tail as impressive as that seen in FGC 1287 by direct ram pressure stripping we would expect a ram pressure force comparable to that of most extreme ongoing ram pressure stripping cases near cluster cores, i.e., ram pressure from a combination of gas densities comparable to ICM in rich clusters cores ($n_e = 3 \times 10^{-3}$ cm^3) at a v_{rel} of at least a typical cluster velocity dispersion $\sim$ 1000 km s^{-1}). Even at a v_{rel} of 750 km s^{-1}(which would be hard to explain in a filament where the expected velocity dispersion is $\sim$ 250 km s^{-1}), the time required to cover the projected distance between FGC 1287 and the filament would be $\sim$ 1 Gyr during which time the H I in the tail would be expected to have either been lost or fallen back into the group or FGC 1287 gravitational potential. As this is not what is observed, this mechanism seems unlikely.

4.5 Evidence for a recent interaction

FGC 1287's warped H I disk (Figure 4) presents the clearest evidence of an interaction within the last $\sim$ 0.7 Gyr, the H I relaxation time–scale for major mergers (Holwerda et al. 2011). The closed velocity contours in the velocity field

of CGCG 097-041, at velocities similar to the warp in FGC 1287, and its morphology, being more extended towards the East (Figure 4) could be the result of an interaction with FGC 1287. The time scale for this interaction assuming a separation velocity of $\sim$250 km s^{-1} would be $\sim$ 0.4 Gyr, i.e., within the H I relaxation time scale for both galaxies. However, this does not provide definitive evidence of a recent tidal interaction.

Supporting evidence for a recent interaction comes from the star formation history derived from the FGC 1287 SDSS spectrum using the Fitting Analysis using Differential evolution Optimization (FADO) spectral synthesis code (Gomes & Papaderos 2017), which shows a spike of star formation a few $\times$ 10^7 years ago. Unfortunately, this interaction time scale is not precise enough to discriminate between the direct and combined gravitational and hydrodynamic stripping scenarios. For now, all we can say is that the FGC 1287 H I disk has suffered a recent and strong interaction which could have been either tidal or hydrodynamic.

There are examples of galaxy flybys creating long HI tails in the literature, e.g, Serra et al. (2013). Although, in that case, the H I tail mass is an order of magnitude lower and more diffuse (without star formation) than for FGC 1287. In the Serra et al. (2013) case, tidal H I stripping was thought to arise from an encounter between NGC 3187 with either the gravitational potential of the group or the group member NGC 3162. For the FGC 1287 H I tail we could not identify a flyby companion. However, an interaction amongst the triplet
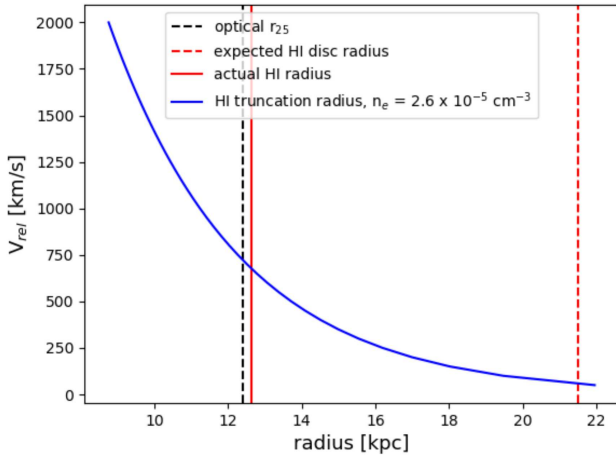
Figure 9. FGC 1287 H I truncation radius from Steinhauser et al. (2016) in kpc as a function of v_{rel} for an ICM number density upper limit from the *XMM–Newton* X–ray observation of $n_e = 2.6 \times 10^{-5}$ cm^{-3} (blue curve). The vertical lines identified in the legend indicate that the H I disk has been truncate down to the optical r_{25} radius.

members (possibly one of them joining the other two) with the gravitational potential of the group might explain the observed kinematics and the change in projected direction midway along the tail.

4.6 Star formation in the H I tail

Perhaps one of the most unexpected results of our analysis is that the VIMOS observations confirmed SF within two of the H I tail clumps, SFC1 and SFC2. Both tail clumps have H I column densities $> 3.1 \times 10^{20}$ atoms cm^{-2}, i.e., above the threshold for SF reported in Maybhate et al. (2007). The stars in the FGC 1287 H I tail are almost certainly formed via in–situ gravitational gas collapse. Given the large H I mass in the FGC 1287 tail, the SFE in the tail appears to be orders of magnitude lower than observed in cluster core Jellyfish/RPS galaxies, e.g., A2667 and A1689, where the stellar tails are prominent in optical images. The presence of SF is an interesting aspect of the long H I tail, but it is important to note this is happening away from the relatively highly pressurised ICM cluster core environments where SF in Jellyfish/RPS tails are normally observed. Near cluster cores the high ICM pressure appears to promote the conversion of H I in the tails to the molecular phase which in turn promotes star formation in the tails (Jáchym et al. 2017, 2019; Chen et al. 2020). Although, the exceptional ~ 90 kpc multi–phase RPS tail of JO206 in the low masss cluster IIZW 108 suggested that high v_{rel} and the resulting draping of the ICM magnetic field may be a more important factor than ICM density in promoting star formation in RPS tails (Müller et al. 2021). ICM draping is the process by which as a LTG penetrates a clusters ICM the magnetic fields in the ICM envelope and align around the LTG and it's RPS tail.

5 CONCLUDING REMARKS

In summary, our new observations reveal FGC 1287 has undergone an interaction within the last 0.7 Gyr, but the type of interaction, tidal or RPS, remains unclear. Our Hα+[NII] imaging shows a chain of at least three star–forming knots along the base of the H I tail. FGC 1287 presents the primary signatures of RPS, i.e., a one–sided ionised or neutral gas tail and unperturbed stellar disk. However, the key prerequisite for RPS is the presence of ICM with sufficient density to strip H I from a galaxy's disk at the galaxy's v_{rel}. One–sided RPS tails are normally observed projected in proximity to an ICM with sufficient density to be detected at X–ray wavelengths. But in the case of FGC 1287 it is projected more than one megaparsec from the nearest X–ray detected ICM and the non–detection of X–ray emission from our *XMM–Newton* pointing at the triplet position implies a ICM $n_e < 2.6 \sim 10^{-5}$ cm^{-3}. In a scenario in which the H I in the FGC 1287 disk is directly removed by RPS the *XMM–Newton* upper limit to ICM n_e implies a $v_{rel} > 700$ km s^{-1}. Moreover, although a recent onset of RPS could be explained as the result of the galaxy's recent arrival at the cluster outskirts it hard to envisage how this could have been sufficiently strong to remove the large mass of H I now observed in the tail.

Then, as discussed in Scott et al. (2012), the geometry of the FGC 1287 tail and the lack of signs of strong recent disturbances observed in the optical disks of the other two galaxies make a purely tidal origin for the FGC 1287 tail unlikely as well. A hybrid explanation of pre-processing within the triplet followed by ram pressure stripping of the triplet's poorly bound IGM to produce the H I tail, while speculative, seems a plausible alternative.

This object remains an enigma and is a reminder of how complex the task of isolating environmental processes affecting galaxy evolution is, even for galaxies in relatively moderately dense environments such as filaments and small groups.

is distributed by the National Optical Astronomy Observatory, which is operated by the Association of Universities for Research in Astronomy (AURA) under a cooperative agreement with the National Science Foundation. This research made use of APLpy, an open–source plotting package for Python (Robitaille & Bressert 2012).

DATA AVAILABILITY

The data underlying this article will be shared on reasonable request to the corresponding author.

REFERENCES

Bahcall N. A., 1999, in Dekel A., Ostriker J. P., eds, Formation of Structure in the Universe. p. 135
Bellhouse C., et al., 2019, MNRAS, 485, 1157
Blum R. D., et al., 2016, in American Astronomical Society Meeting Abstracts #228. p. 317.01
Boselli A., Gavazzi G., 2006, PASP, 118, 517
Boselli A., Boissier S., Cortese L., Gil de Paz A., Seibert M., Madore B. F., Buat V., Martin D. C., 2006, ApJ, 651, 811
Boselli A., et al., 2016, A&A, 587, A68
Bravo-Alfaro H., Cayatte V., van Gorkom J. H., Balkowski C., 2000, AJ, 119, 580
Cavaliere A., Fusco-Femiano R., 1976, A&A, 500, 95
Cen R., Tripp T. M., Ostriker J. P., Jenkins E. B., 2001, ApJL, 559, L5
Chen H., et al., 2020, MNRAS, 496, 4654
Chung A., van Gorkom J. H., Kenney J. D. P., Vollmer B., 2007, ApJL, 659, L115
Chung A., van Gorkom J. H., Kenney J. D. P., Crowl H., Vollmer B., 2009, AJ, 138, 1741
Consolandi G., Gavazzi G., Fossati M., Fumagalli M., Boselli A., Yagi M., Yoshida M., 2017, A&A, 606, A83
Cortese L., Gavazzi G., Boselli A., Iglesias-Paramo J., Carrasco L., 2004, A&A, 425, 429
Cortese L., Gavazzi G., Boselli A., Franzetti P., Kennicutt R. C., O'Neil K., Sakai S., 2006, A&A, 453, 847
Cortese L., et al., 2007, MNRAS, 376, 157
Cortese L., et al., 2008, MNRAS, 383, 1519
Cortese L., et al., 2012, A&A, 544, A101
Cortese L., Catinella B., Smith R., 2021, PASA, 38, e035
Denicoló G., Terlevich R., Terlevich E., 2002, MNRAS, 330, 69
Di Teodoro E. M., Fraternali F., 2015, MNRAS, 451, 3021
Dressler A., 2004, in Mulchaey J. S., Dressler A., Oemler A., eds, Clusters of Galaxies: Probes of Cosmological Structure and Galaxy Evolution. p. 206
Gavazzi G., Jaffe W., 1987, A&A, 186, L1
Gavazzi G., Contursi A., Carrasco L., Boselli A., Kennicutt R., Scodeggio M., Jaffe W., 1995, A&A, 304, 325
Gavazzi G., Boselli A., Mayer L., Iglesias-Paramo J., Vílchez J. M., Carrasco L., 2001, ApJL, 563, L23
Ge C., et al., 2021, MNRAS, 505, 4702
Gomes J. M., Papaderos P., 2017, A&A, 603, A63
Gorenstein P., Fabricant D., Topka K., Harnden F. R. J., Tucker W. H., 1978, ApJ, 224, 718
Gunn J. E., Gott J. R. I., 1972, ApJ, 176, 1
Heesen V., Brinks E., Leroy A. K., Heald G., Braun R., Bigiel F., Beck R., 2014, AJ, 147, 103
Hester J. A., et al., 2010, ApJL, 716, L14
Holwerda B. W., Pirzkal N., Cox T. J., de Blok W. J. G., Weniger J., Bouchard A., Blyth S.-L., van der Heyden K. J., 2011, MNRAS, 416, 2426
Jáchym P., et al., 2017, ApJ, 839, 114

Jáchym P., et al., 2019, ApJ, 883, 145
Keenan O. C., Davies J. I., Taylor R., Minchin R. F., 2016, MNRAS, 456, 951
Kennicutt Jr. R. C., 1998, ARA&A, 36, 189
Kleiner D., et al., 2021, A&A, 648, A32
Lagos P., Demarco R., Papaderos P., Telles E., Nigoche-Netro A., Humphrey A., Roche N., Gomes J. M., 2016, MNRAS, 456, 1549
Lagos P., Scott T. C., Nigoche-Netro A., Demarco R., Humphrey A., Papaderos P., 2018, MNRAS, 477, 392
Lee J., Kimm T., Katz H., Rosdahl J., Devriendt J., Slyz A., 2020, ApJ, 905, 31
Macquart J. P., et al., 2020, Nature, 581, 391
Maybhate A., Masiero J., Hibbard J. E., Charlton J. C., Palma C., Knierman K. A., English J., 2007, MNRAS, 381, 59
McMullin J. P., Waters B., Schiebel D., Young W., Golap K., 2007, in Shaw R. A., Hill F., Bell D. J., eds, Astronomical Society of the Pacific Conference Series Vol. 376, Astronomical Data Analysis Software and Systems XVI. p. 127
Moretti A., et al., 2020, ApJ, 889, 9
Moss C., 2006, MNRAS, 373, 167
Müller A., et al., 2021, Nature Astronomy, 5, 159
Poggianti B. M., et al., 2017, ApJ, 844, 48
Poggianti B. M., et al., 2019, MNRAS, 482, 4466
Poggianti B. M., et al., 2020, ArXiv 170310301Y, p. arXiv:2005.03735
Ramatsoku M., et al., 2019, MNRAS, 487, 4580
Reynolds T. N., et al., 2021, MNRAS, 505, 1891
Robitaille T., Bressert E., 2012, APLpy: Astronomical Plotting Library in Python, Astrophysics Source Code Library (ascl:1208.017)
Roediger E., Brüggen M., 2007, MNRAS, p. 765
Scott T. C., et al., 2010, MNRAS, 403, 1175 (Paper I)
Scott T. C., Cortese L., Brinks E., Bravo-Alfaro H., Auld R., Minchin R., 2012, MNRAS, 419, L19 (Paper II)
Scott T. C., Brinks E., Cortese L., Boselli A., Bravo-Alfaro H., 2018, MNRAS, 475, 4648
Serra P., et al., 2013, MNRAS, 428, 370
Serra P., et al., 2015, MNRAS, 448, 1922
Smith R. J., et al., 2010, MNRAS, 408, 1417
Solanes J. M., Manrique A., García-Gómez C., González-Casado G., Giovanelli R., Haynes M. P., 2001, ApJ, 548, 97
Speagle J. S., Steinhardt C. L., Capak P. L., Silverman J. D., 2014, ApJS, 214, 15
Spergel D. N., et al., 2007, ApJS, 170, 377
Steinhauser D., Schindler S., Springel V., 2016, A&A, 591, A51
Sun M., Donahue M., Roediger E., Nulsen P. E. J., Voit G. M., Sarazin C., Forman W., Jones C., 2010, ApJ, 708, 946
Tamburro D., Rix H. W., Leroy A. K., Mac Low M. M., Walter F., Kennicutt R. C., Brinks E., de Blok W. J. G., 2009, AJ, 137, 4424
Tempel E., Tago E., Liivamägi L. J., 2012, A&A, 540, A106
Vikhlinin A., Forman W., Jones C., 1999, ApJ, 525, 47
Vollmer B., Balkowski C., Cayatte V., van Driel W., Huchtmeier W., 2004, A&A, 419, 35
Wang J., Koribalski B. S., Serra P., van der Hulst T., Roychowdhury S., Kamphuis P., Chengalur J. N., 2016, MNRAS, 460, 2143
Yagi M., et al., 2010, AJ, 140, 1814
Yagi M., Yoshida M., Gavazzi G., Komiyama Y., Kashikawa N., Okamura S., 2017, ApJ, 839, 65
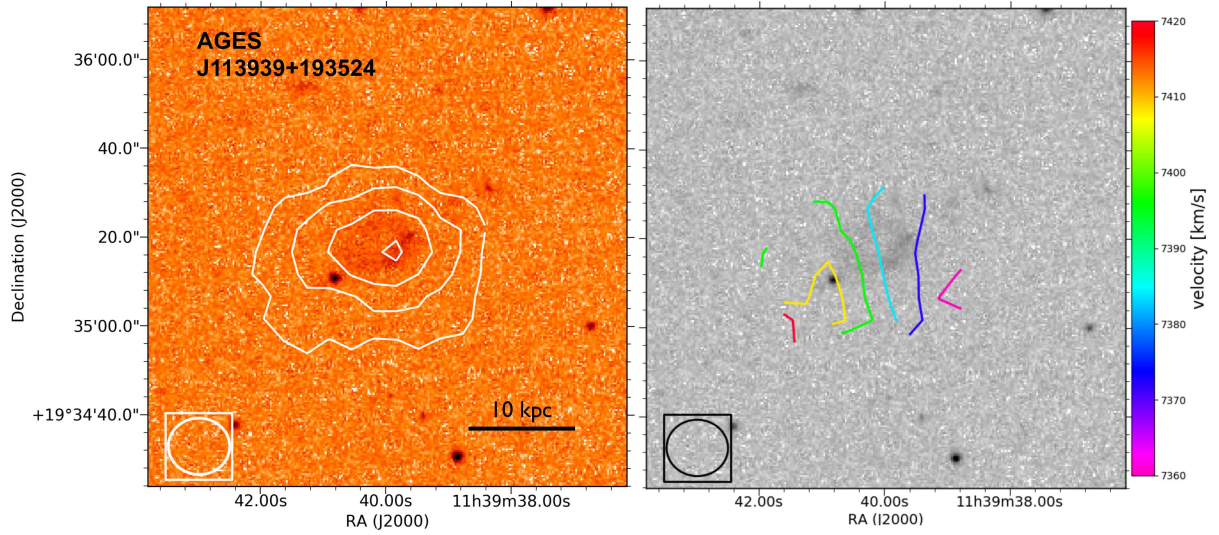Yoshida M., et al., 2008, ApJ, 688, 918

Figure A1. AGES J113939+193524 (SDSS J113939.67+193516.7): *left* VLA B/C–configuration H I column density contours (in white). The contours are at H I column densities of 0.5, 1.6, 3.1, and 4.7×10^{20} atom cm^{-2}. *Right* H I velocity field with contours separated by 10 km s^{-1}. The background images are SDSS g–band. The boxed ellipse at the bottom left of each panel shows the size (13.84 × 12.69 arcsec) and orientation of the VLA beam.
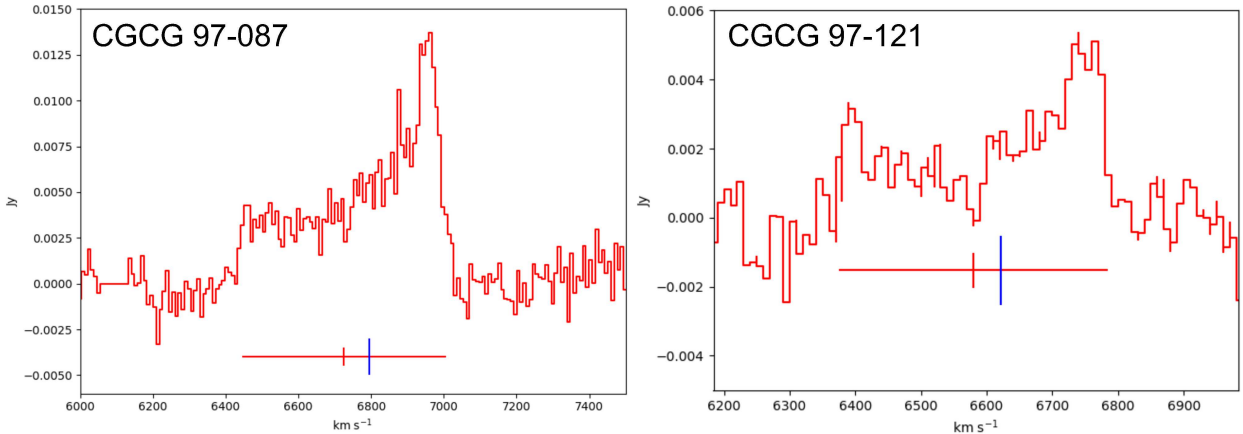

Figure B1. AGES H I profiles for CGCG 097-087 (left) and CGCG 097-121 (right). The red horizontal bar at the base of each spectrum delimits W$_{20}$ with the red vertical bars indicating V$_{HI}$ based on mean W$_{20}$ velocities and the blue vertical bars indicating the flux weighed V$_{HI}$.

APPENDIX A:

H I was detected in AGES J113939+193524 (SDSS J113939.67+193516.7) in the FGC 1287 VLA field of view. SDSS J113939.67+193516.7 is projected ~ 178 kpc east of FGC 1287. Figure A1 shows the H I column density and velocity field for the galaxy.

APPENDIX B:

Figure B1 shows the AGES H I profiles of CGCG 097-087 (left) and CGCG 097-121 (right) which are A 1367 LTGs displaying one–sided H I tails in their VLA integrated maps (Scott et al. 2010, 2018). The A_{flux} H I asymmetry measurement for the galaxies are 1.82±0.09 and 1.92±0.08 respectively; both are projected within 550 kpc of the cluster centre.